Journal of the Korean Crystal Growth and Crystal Technology
Vol. 31, No. 3 (2021) 127-136
https://doi.org/10.6111/JKCGCT.2021.31.3.127

p-ISSN 1225-1429
e-ISSN 2234-5078

# Studies on Nusselt and Sherwood number for diffusion-advective convection during physical vapor transport of $Hg_2Br_2$

Geug Tae Kim† and Moo Hyun Kwon*

*Department of Chemical Engineering, Hannam University, Daejeon 34054, Korea*
**Department of Energy and Electrical Engineering, Woosuk University, Jincheon 27841, Korea*

(Received May 28, 2021)
(Revised June 14, 2021)
(Accepted June 15, 2021)

**Abstract** This paper is dedicated to numerical simulation for diffusion-advective convection in a square cavity during physical vapor transport of $Hg_2Br_2$. Flow characteristics of the temperature difference between the source and crystal regions, 50°C (300°C → 250°C), partial pressures of component argon of 20 Torr and 100 Torr are investigated and presented as velocity vectors and streamlines, isotherms and iso-mass concentrations contours. Moreover, alterations of average Nusselt and average Sherwood numbers with (a) the source and crystal regions, (b) the pressures of component argon of 20 Torr and 100 Torr are analyzed and addressed in details. Both average Nusselt and average Sherwood numbers are seen to decrease with the increasing values of the partial pressures of component argon. Also, it is found that for the two different partial pressures of component argon, average Nusselt numbers at the source region are greater than at the crystal region, and inversely, average Sherwood numbers at the crystal region are greater than the source region by a factor of 3.

**Key words** Diffusion-advection, Nusselt number, Sherwood number, Physical vapor transport, $Hg_2Br_2$

## 1. Introduction

Double diffusive convection is a transport phenomenon associated with a buoyancy driven motion which emerges as a consequence of the gravity and the density variations from both thermal and concentration gradients, and is referred to as thermo-solutal convection, or combined natural convection heat and mass transfer. Yang and Zhao [1] carried out 2D numerical study of double diffusive convection in rectangular cavities with various aspect ratios (height-to-width). In most recent years, extensive researches on double diffusive convection in the porous problems have been performed [2-10]. The heat and mass transfer in double diffusion natural convection associated nanofluids are investigated [11,12]. Liu et al. [13] reported that the Dufour and Soret effects with double-diffusive convection utilizing multiple-relaxation-time lattice Boltzmann model. Chakkingal et al. [14] dealt that the heat and mass transfer in a cubical enclosure with adiabatic cylindrical obstacles. Meften [15] addressed that conditional and unconditional stability for double diffusive convection. Hamimid et al. [16] investigated the limit of the buoyancy ratio for double diffusive convection in binary mixture and Chauhan et al. [17] studied the effect viscous dissipation on double diffusive convection in a square cavity.

When a mass flux into the enclosure occurs at the hot end wall due to either the sublimation of a solid or evaporation of a liquid (species A), and condensation of species A occurs at the opposite cold wall end wall, combined natural convection by thermal and solutal gradients across the enclosure (double diffusive convection) and a mass flux at the surfaces (advection) occur simultaneously and this mode of transfer is referred as a diffusive advection convection. An inert carrier gas (species B) which is not soluble in species A (solid or liquid) is present in the enclosure. For a typical example, the transport phenomena in a crystal growth system by the physical vapor transport (PVT) corresponds to diffusive-advective convection. Kim and his coworkers [18-21] and Duval [22] have performed numerical simulations of diffusive-advective convection in the vapor crystals of mercurous halides grown by the physical vapor transport (PVT). Weaver and Viskanta [23,24] carried out systematically 2D numerical simulations of diffusive-advection convection based on evaporation and condensation from an application standpoint.

Mercurous halide materials are well known as the most promising materials in applications for acousto-optic materials and signal processing optics, for example, Bragg cells. In particular, $Hg_2Br_2$ crystals have drawn

†Corresponding author
E-mail: geugtaekim@gmail.com

much attention due to their excellent acousto-optic properties in the field of spectral imaging and optical processing. Singh and his group investigated systematically the growth and characterization and development of large single crystals of $Hg_2Br_2$ [25-34]. Most recent reports of $Hg_2Br_2$ could be found in references [35,36]. Liu et al [37] presented that he growth of high-quality $Hg_2Br_2$ crystals is critical for the characterization of crystal properties and the fabrication of acousto-optic devices. They successfully prepared high-quality $Hg_2Br_2$ crystals with the size of 35 mm in diameter and 40 mm in length by physical vapor transport method.

Our numerical simulations are motivated by the desire to study on how heat and mass transfer phenomena in the diffusive-advective natural convection would tend to influence the dimensionless Nusselt (Nu) and Sherwood number (Sh) during convection for $Hg_2Br_2$ vapor growth by the physical vapor transport in a differentially heated square cavity. Furthermore, a discussion of the flow characteristics in terms of the streamline profiles, isotherm, iso-mass concentration contours is also presented. Finally, from an application standpoint, a simple correlation of the average Nusselt number and average Sherwood number with the partial pressure of component B (argon as inert gas), $P_B$ is presented, which can be used for the interpolation of the present results for the intermediate values of the governing transport parameters in a new application.

## 2. Mathematical Formulation of the Problem

Consider a PVT (physical vapor transport) crystal growth in a square cavity with differentially heated end walls with a linear temperature profile, as shown in Fig. 1. Sublimation of $Hg_2Br_2$ (species A) occurs at the hot end wall (source region) with a temperature $T_s$, and vapor of $Hg_2Br_2$ (species A) is transported into the vapor region, and condensation of vapor of $Hg_2Br_2$ (species A) occurs at the opposite cold end wall (crystal region) with a temperature $T_c$, $T_s > T_c$. An inert carrier gas, argon (species B) which is not soluble in $Hg_2Br_2$ (species A) exists in the vapor region within the enclosure. Therefore, diffusive-advective convection is the mode of buoyancy driven fluid motion by thermal and solutal gradients across the PVT growth enclosure on earth. In the system considered in this study, there are no chemical reaction, heat generation or heat dissipation, and the system is at steady state. The fluid motion is assumed laminar and radiation heat transfer in the enclosure is assumed to be negligible.

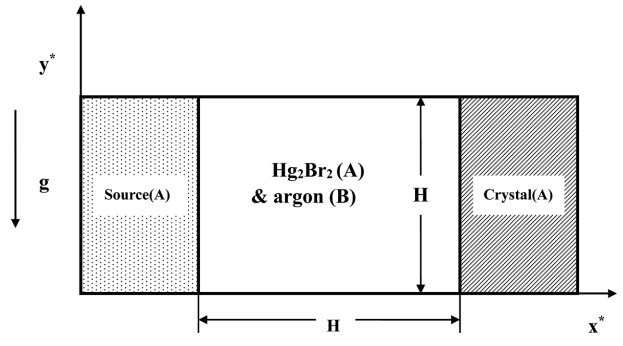


Fig. 1. System schematic and coordinates for numerical simulation of PVT crystal growth square cavity of $Hg_2Br_2$(A)-argon (B).

### *2.1. Dimensionless form of Equations*

The thermo-physical properties (density ρ, kinematic viscosity n, thermal conductivity k, thermal diffusivity a, and binary mass diffusivity $D_{AB}$) are scaled, respectively, by $\rho_0$, $\nu_0$, $k_0$, $\alpha_0$, $D_{AB,0}$, where the subscript 0 denotes vales at the reference temperature $T_0$ and the reference mass fraction $\omega_0$. $T_0 = (T_h + T_c)/2$, and $\omega_0 = (\omega_{A,s} + \omega_{A,c})/2$ are used in this study.

The dimensionless quantities are:
$x^* = x/H$, $y^* = y/H$, $u = v_x/U$, $v = v_y/U$,
$p^* = p/r_0U^2$, $T^* = (T - T_c)/(T_h - T_c)$,
$\omega^*_A = (\omega_A - \omega_{A,c})/(\omega_{A,s} - \omega_{A,c})$, $U = \alpha/H$,

where U is the characteristic velocity and H is the cavity height, and x, y are Cartesian coordinate directed along the length and height of the cavity, respectively, and p is the pressure.

The resulting conservation equations of mass, momentum, energy and species are given in dimensionless form as follows:

$$\nabla^* \bullet \vec{V} = 0, \tag{1}$$

$$\vec{V} \bullet \nabla^* \vec{V} = -\nabla^* p^* + Pr\nabla^{*2}\vec{V} - Gr \bullet Pr^2 \frac{(1-\rho^*)}{\beta\Delta T}, \tag{2}$$

$$\vec{V} \bullet \nabla^* T^* = \nabla^{*2} T^*, \tag{3}$$

$$\vec{V} \bullet \nabla^* \omega_A^* = \frac{1}{Le}\nabla^{*2}\omega_A^*. \tag{4}$$

The corresponding dimensionless boundary conditions are given as follows:

On the walls
$(0 < x^* < 1, y^* = 0$ and $1)$:

$$u(x^*, 0) = u(x^*, 1) = v(x^*, 0) = v(x^*, 1) = 0 \quad (5)$$

$$\frac{\partial \omega_A^*(x^*, 0)}{\partial y^*} = \frac{\partial \omega_A^*(x^*, 1)}{\partial y^*} = 0,$$

$$T^*(x^*, 0) = -x^* + 1.$$

On the source ($x^* = 0$, $0 < y^* < 1$):

$$u(0, y^*) = -\frac{1}{Le(C_v - 1)} \frac{\partial \omega_A^*(0, y^*)}{\partial x^*}, \quad (6)$$

$$v(0, y^*) = 0,$$
$$T^*(0, y^*) = 1,$$
$$\omega_A^*(0, y^*) = 1.$$

On the crystal ($x^* = 1$, $0 < y^* < 1$):

$$u(1, y^*) = -\frac{1}{Le(C_v - 1)} \frac{\partial \omega_A^*(1, y^*)}{\partial x^*}, \quad (7)$$

$$v(1, y^*) = 0,$$
$$T^*(1, y^*) = 1,$$
$$\omega_A^*(1, y^*) = 1.$$

### *2.2. Dimensionless Governing Transport Parameters*

The above governing equations indicate that the present problem is governed by six dimensionless parameters, namely, Prandtl number, Lewis number, Peclet number, concentration number, thermal Grashof number, solutal Grashof number. The dimensionless governing transport parameters are listed as follows:

$Pr = \nu/\alpha$, Prandtl number,
$Le = D_{AB}/\alpha$, Lewis number,
$Pe = U_{adv}H/D_{AB}$, Peclet number,
$C_v = 1 - \omega_{A,c}/(\omega_{A,s} - \omega_{A,c})$ concentration number,
$Gr_t = \rho g \beta_t \Delta T H^3/\alpha\nu$, thermal Grashof number,
$Gr_s = \rho g \beta_s \Delta\omega H^3/\alpha\nu$, solutal Grashof number,

where $\beta_t$ and $\beta_s$ are the thermal expansion coefficient and the solutal expansion coefficient, $\beta_t = (-1\rho_0/)(\partial\rho/\partial T)|_{\omega 0}$ and $\beta_s = = (-1\rho_0/)(\partial\rho/\partial\omega)|_{T0}$, respectively, and $U_{adv}$ is the characteristic velocity based on the diffusion-driven advection. The subscript A, s, c denote the mass species $Hg_2Br_2$, the source region and crystal region, respectively.

The heat and mass transfer of the diffusive-advective convection in the cavity can be characterized in terms of the local $Nu_y$ and Sherwood number $Sh_y$, which are defined as:

$Nu_y = hH/k$,
$Sh_y = h_mH/\rho\ D_{AB}$

where h and $h_m$ are heat transfer convection coefficient and mass transfer convection coefficient, respectively.

The average convective Nusselt and Sherwood number are calculated by integrating the temperature and mass concentration gradient over the height wall as

$$Nu = -\int Nu_y\,(y^*)\,dy^*,$$
$$Sh = -\int Sh_y\,(y^*)\,dy^*$$

The Nusselt number is the total heat flux over the heat flux due to heat conduction alone across the enclosure. In other words, the dimensionless diffusive-convection energy flux will be denoted by

$$Q_d = -(\partial T^*/\partial x^*)|_{T^* = 0}$$

$Q_d$ illustrates the increased heat transfer at the wall due to double-diffusive convection. With a mass flux at the wall, energy is transported at the surface by advection of fluid into or out of the cavity. Therefore, the total energy transferred at the wall includes contributions from diffusion and advection. Hence, the Nusselt number is defined as

$$Nu_y = -(\partial T^*/\partial x^*)|_{T^* = 0} + \rho^* u T^*,$$
$$\text{or } Nu = (Q_d + Q_a)$$

where $Q_a = \rho^* u T^*$ is the dimensionless energy flux due to advection [23].

Similarly, the Sherwood number at the wall is defined as the mass transfer over the mass transfer due to only diffusion in the cavity. In the absence of natural convection, the concentration field is diffusion dominated, and the Sherwood number is equal to unity. If no mass transfer occurs at the wall, the Sherwood number vanishes because the concentration gradient would zero. The Sherwood number illustrates the increased mass transfer (concentration gradient) at the wall due to natural convection effects [23].

$$Sh_y = h_mH/\rho\ D_{AB} = (1/(1 - (\omega^*\Delta\omega + \omega_A))\ (\partial\omega^*/\partial x^*)|_{x^* = 0}$$

Note that the diffusion advective mass flux at the interface between the vapor and the wall which can be expressed by $[\rho\ D_{AB}/(1 - \omega)](\partial\omega/\partial x)|_{x\ =\ 0} = h_m(\omega_{A,s} - w_{A,c})$, and the local Sherwood number can be derived.

### *2.3. Method of Solution*

The Semi-Implicit Method Pressure-Linked Equations Revised (SIMPLER) [38] based on the finite volume procedure was utilized to solve all the governing equations, namely, continuity, momentum, energy, and mass concentration equations along with boundary con-

Table 1
Thermo-physical properties of $Hg_2Br_2$(A)-argon (B) ($M_A$ = 560.988, $M_B$ = 39.944) at $\Delta T = 50^oC$

| Parameter | $P_B$ = 20 Torr | $P_B$ = 100 Torr |
|---|---|---|
| Kinematic viscosity | 0.44 $cm^2/sec$ | 0.40 $cm^2/sec$ |
| Thermal diffusivity | 0.45 $cm^2/sec^2$ | 0.45 $cm^2/sec^2$ |
| Binary diffusivity | 1.17 $cm^2/sec^2$ | 0.70 $cm^2/sec^2$ |
| Coefficient of thermal volume expansion | 0.0017 ($1/^oC$) | 0.0017 ($1/^oC$) |
| Density of mixture | 0.0006 $g/cm^3$ | 0.0007 $g/cm^3$ |
| Prandtl number | 0.96 | 0.89 |
| Lewis number | 0.38 | 0.64 |
| Peclet number | 3.03 | 1.85 |
| Concentration number | 1.05 | 1.18 |
| Thermal Grashof number | $3.54 \times 10^3$ | $4.14 \times 10^3$ |
| Solutal Grashof number | $4.95 \times 10^4$ | $5.29 \times 10^4$ |

ditions. The current code was validated with previously published results in references [18,19].

## 3. Results and Discussion

For $M_A \neq M_B$, the molecular weights of $Hg_2Br_2$ ($M_A$ = 560.988 g/gmol), and the molecular weights of argon ($M_B$ = 39.944 g/gmol), the transport phenomena in the vapor phase are much complicated. Firstly, thermal and/or solutal buoyancy-driven convection are coupled. Secondly, the effects of advection which reflect the mass flux of $Hg_2Br_2$ (A) in the source and crystal interfaces cannot be neglected during the physical vapor transport of $Hg_2Br_2$ in the vapor phase. This study is mainly focused on the relations of the Nusselt and Sherwood numbers for two different partial pressures of component argon (B), $P_B$ = 20 Torr, and 100 Torr, at the source and crystal interfaces. Thermo-physical properties of $Hg_2Br_2$ (A)-argon (B) ($M_A$ = 560.988, $M_B$ = 39.944) at $\Delta T = 50^oC$, $P_B$ = 20 Torr and 100 Torr used in this study are listed in Table 1.

As shown in Fig. 2, it is clear that at the right hot wall (the source region), the dimensionless local Nusselt number, $Nu_y$ increases with the dimensionless coordinate along the y-direction, $y^*$ for diffusion-advection and convection plus diffusion-advection, and remains almost constant for $0 \le y^* \le 1$ for natural convection, based on Ar (width-to-transport length) = 1, $\Delta T = 50^oC$ ($300^oC \rightarrow 250^oC$), $P_B$ = 20 Torr, thermal Grashof number ($Gr_t$) = $3.54 \times 10^3$, solutal Grashof number ($Gr_s$) = $4.95 \times 10^4$, Prandtl number (Pr) = 0.96, Lewis number (Le) = 0.38, Peclet number (Pe) = 3.03, concentration parameter ($C_v$) = 1.05, on earth. The dimensionless local Nusselt number, $Nu_y$ for diffusion-advection is much

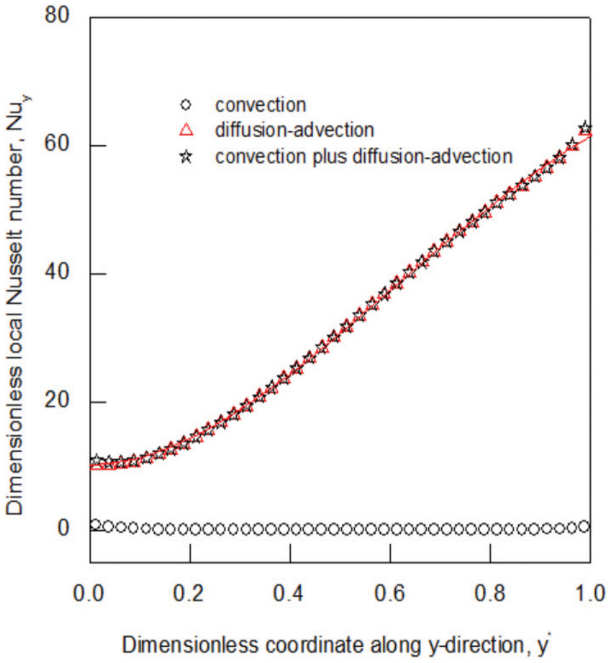


Fig. 2. Dimensionless local Nusselt number, $Nu_y$ for dimensionless coordinate along the y-direction, $y^*$ at the right hot wall (the source region), based on Ar = 1, $\Delta T = 50^oC$ ($300^oC \rightarrow 250^oC$), $P_B$ = 20 Torr, thermal Grashof number ($Gr_t$) = $3.54 \times 10^3$, solutal Grashof number ($Gr_s$) = $4.95 \times 10^4$, Prandtl number (Pr) = 0.96, Lewis number (Le) = 0.38, Peclet number (Pe) = 3.03, concentration parameter ($C_v$) = 1.05, on earth.

Table 2
Summary of average Nusselt number and average Sherwood number

| | $P_B$ = 20 Torr | | $P_B$ = 100 Torr | |
|---|---|---|---|---|
| | Source | Crystal | Source | Crystal |
| Average Nusselt number, Nu | 32.3 | 27.6 | 14.0 | 11.1 |
| Average Sherwood number, Sh | 17.1 | 54.9 | 10.5 | 30.4 |

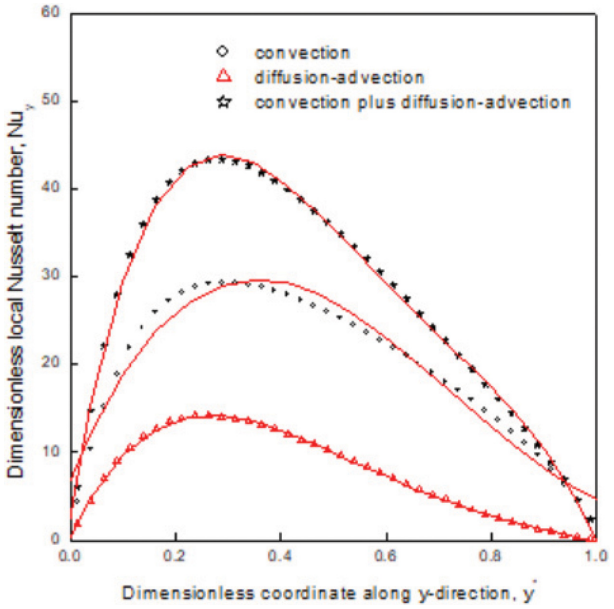


Fig. 3. Dimensionless local Nusselt number, $Nu_y$ for dimensionless coordinate along the y-direction, $y^*$ at the left cold wall (the crystal region). Note that the transport parameters in Fig. 3 for $P_B$ = 20 Torr are the same as in Fig. 2.

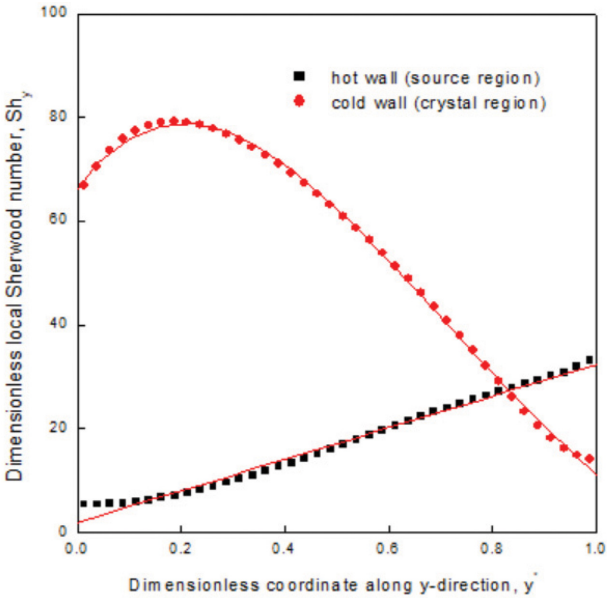


Fig. 4. Dimensionless local Sherwood number, $Sh_y$ for dimensionless coordinate along the y-direction, $y^*$ at (a) the right hot wall (the source region) and (b) the left cold wall (the crystal region). Note that the transport parameters in Fig. 4 for $P_B$ = 20 Torr are the same as in Fig. 2.

greater that for convection alone by one order of magnitude. As shown in Table 2, the average Nusselt number at the right hot wall (the source region), Nu = 32.3. Figure 3 shows the dimensionless local Nusselt number, $Nu_y$ for dimensionless coordinate along the y-direction, $y^*$ at the left cold wall (the crystal region), with same transport parameters as in Fig. 2. At the crystal region, the dimensionless local Nusselt number, $Nu_y$ for convection is greater that for diffusion-advection alone by a factor of 2. The dimensionless local Nusselt number, $Nu_y$ changes with the dimensionless coordinate along y-direction, $y^*$ and exhibits an asymmetrical parabolic pattern. As shown in Table 2, the average Nusselt number at the left cold wall (the crystal region), Nu = 27.6. It is found that the average Nusselt numbers at the source region are slightly greater than at the crystal region.

Figure 4 shows the dimensionless local Sherwood number, $Sh_y$ for dimensionless coordinate along the y-direction, $y^*$ at (a) the right hot wall (the source region) and (b) the left cold wall (the crystal region). The dimensionless local Sherwood number, $Sh_y$ along the y-direction, $y^*$ at the left cold wall (the crystal region) is greater than at the right hot wall (the source region). As shown in Table 2, the average Sherwood number at the right hot wall (the source region) and the left cold wall (the crystal region) are Sh = 17. 1 and 54.9, respectively. As seen in Figs. 2 through 4 and Table 2, the source and crystal region have an inverse relationship with average Nusselt and average Sherwood numbers.

Figure 5 shows velocity vectors, streamlines, iso-temperature, iso-mass concentration contours. To show the velocity field inside the square cavity, streamlines along with the velocity vectors are also presented, with $|U|_{max}$ = 22.23 cm/sec. The dimensional maximum magnitude of velocity vectors represents an intensity of convection inside the square cavity. It is found that single one convective roll is present in the vapor phase. The flow structure is asymmetrical against at y* = 0.5 and three-dimensional flow structure. For the flow regions along the transport length at the bottom region, i.e., $0 \le y^* \le 0.5$, the one-dimensional Stefan flows appear. Temperature profile shown in Fig. 5(c) is related to the linear thermal boundary conditions, for $0 \le x^* \le 1$, conductive walls. Close spacings of mass concentration shown in Fig. 5(d) exhibits the mechanism of the diffusion-limited mass transfer. If the interface kinetics are sufficiently fast, the actual interface vapor pressure equals the saturation vapor pressure. In other words, when the mass transport is rate-limiting (or rate-determining or rate-controlling) step, the actual vapor pressure at the interface is close to the saturation pressure at the growing crystal. Therefore, close spacings of mass concentration reflects the resistance of mass transport due to diffusion. Note the transport parameters in Figs. 3 through 5 for $P_B$ = 20 Torr are the same as in Fig. 2.

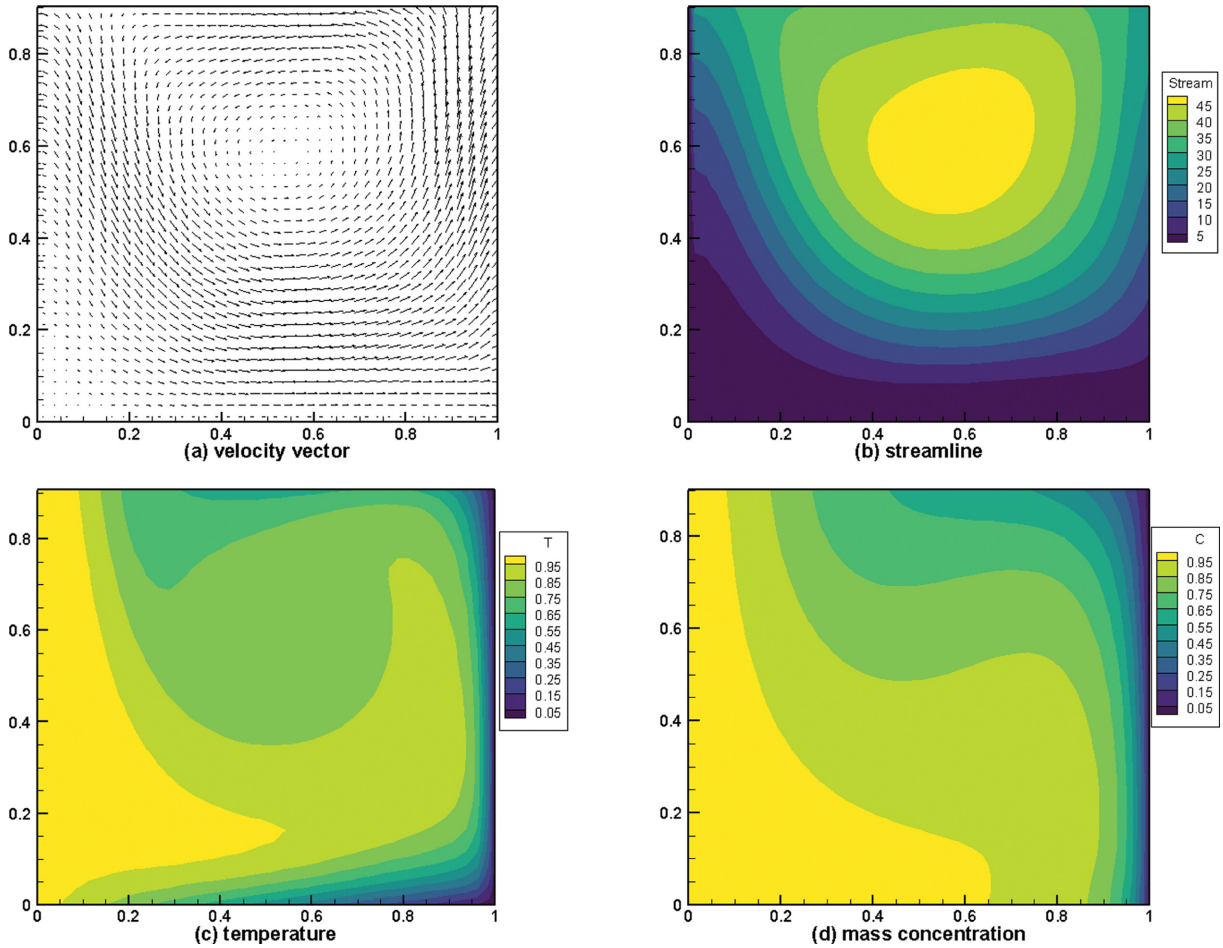


Fig. 5. (a) velocity vector, (b) streamline, (c) temperature, (d) mass concentration profile. Note that the transport parameters in Fig. 5 for $P_B = 20$ Torr are the same as in Fig. 2. $|U|_{max} = 22.23$ cm/sec.

Figure 6 shows that at the right hot wall (the source region), the dimensionless local Nusselt number, $Nu_y$ increases with the dimensionless coordinate along the y-direction, y* for the two different partial pressure of component B (argon), $P_B$ = 20 Torr and $P_B$ = 100 Torr. At the source region, the dimensionless local Nusselt number for the pressures of component argon of 20 Torr is greater than for 100 Torr. At the right hot wall (the source region), the dimensionless local Nusselt number, $Nu_y$ linearly and directly increases with the dimensionless coordinate along the y-direction, y*.

Figure 7 shows that at the left cold wall (the crystal region), the dimensionless local Nusselt number, $Nu_y$ increases with the dimensionless coordinate along the y-direction, y* for the two different partial pressure of component B (argon), $P_B$ = 20 Torr and $P_B$ = 100 Torr. In Figs. 6 and 7, the corresponding transport parameters for the case of $P_B$ = 100 Torr are thermal Grashof number ($Gr_t$) = $4.14 \times 10^3$, solutal Grashof number ($Gr_s$) = $5.29 \times 10^4$, Prandtl number (Pr) = 0.89, Lewis number (Le) = 0.64, Peclet number (Pe) = 1.85, concentration parameter ($C_v$) = 1.18, on earth. Ar (width-to-transport length) = 1 and $\Delta T = 50^oC$ ($300^oC \rightarrow 250^oC$) are fixed. In the same trend, at the crystal region, the dimensionless local Nusselt number for the pressures of component argon of 20 Torr is greater than for 100 Torr. At the left cold wall (the crystal region), the dimensionless local Nusselt number, $Nu_y$ for $P_B$ = 20 Torr and $P_B$ = 100 Torr, first increases steeply up to a critical value of the local Nusselt number Nu = 43 and 18, respectively, and beyond the position near y* = 0.3, decreases as the dimensionless coordinate along the y-direction, y* further increases. The profile of the dimensionless local Nusselt number, $Nu_y$ is asymmetrical parabolic. The dissimilar pattern of dimensionless local Nusselt numbers for source and crystal region in Figs. 6 and 7 is likely to occur from the mass flux at interfaces, but at this point, remains unsolved problems for further researches.

Figure 8 shows that for the two different partial pres-

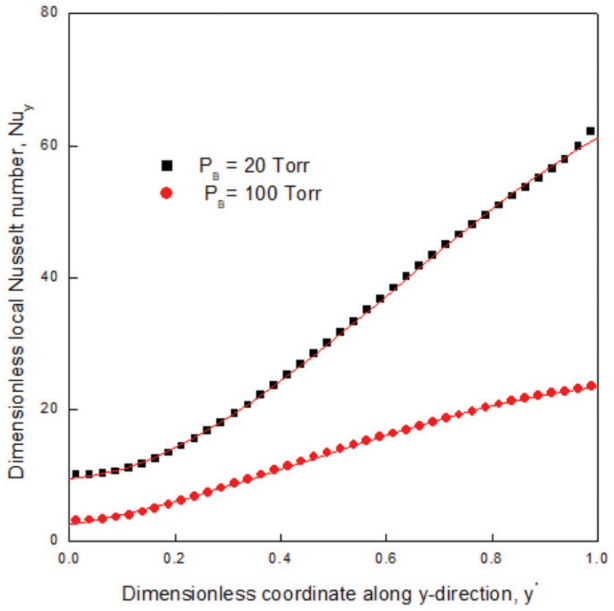


Fig. 6. Dimensionless local Nusselt number (heat flux due to convection plus diffusion-advection), $Nu_y$ for dimensionless coordinate along the y-direction, y* at the right hot wall (the source region), for (a) $P_B = 20$ Torr, thermal Grashof number $(Gr_t) = 3.54 \times 10^3$, solutal Grashof number $(Gr_s) = 4.95 \times 10^4$, Prandtl number (Pr) = 0.96, Lewis number (Le) = 0.38, Peclet number (Pe) = 3.03, concentration parameter $(C_v) = 1.05$; (b) $P_B = 100$ Torr, thermal Grashof number $(Gr_t) = 4.14 \times 10^3$, solutal Grashof number $(Gr_s) = 5.29 \times 10^4$, Prandtl number (Pr) = 0.89, Lewis number (Le) = 0.64, Peclet number (Pe) = 1.85, concentration parameter $(C_v) = 1.18$, on earth. Ar = 1 and $\Delta T = 50^oC$ ($300^oC \rightarrow 250^oC$) are fixed.

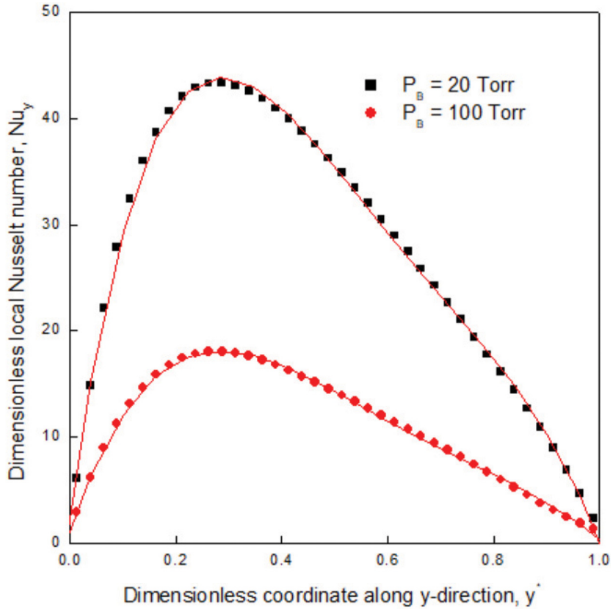


Fig. 7. Dimensionless local Nusselt number, $Nu_y$ for dimensionless coordinate along the y-direction, y* at the left cold wall (the crystal region), for $P_B = 20$ Torr and $P_B = 100$ Torr. Note that the transport parameters in Fig. 7 are the same as in Fig. 6.

sure of component B (argon), $P_B$ = 20 Torr and $P_B$ = 100 Torr, the dimensionless local Sherwood number, $Sh_y$ for dimensionless coordinate along the y-direction, y* at the right hot wall (the source region) and the left cold wall (the crystal region). Note the transport parameters in Fig. 8 are the same as in Fig. 6. The dimensionless local Sherwood numbers, $Sh_y$ for $P_B$ = 20 Torr are greater than for $P_B$ = 100 Torr for both source and crystal regions. In the crystal region, the profile of the dimensionless local Sherwood number, $Sh_y$ is asymmetrical parabolic for both $P_B$ = 20 Torr and $P_B$ = 100 Torr. On the other hand, in the source region, the dimensionless local Sherwood number, $Sh_y$ a linearly direct relationship with the dimensionless coordinate along the y-direction, y*. As shown in Table 2, the average Sherwood number for $P_B$ = 100 Torr at the right hot wall (the source region) and the left cold wall (the crystal region) are Sh = 10. 5 and 30.4, respectively. For both $P_B$ = 20 Torr and $P_B$ = 100 Torr, the average Sherwood numbers at the crystal region are augmented by a factor of 3 in a comparison with the source region. In other words, Sh = 54.9 ($P_B$ = 20 Torr) and Sh = 30.4 ($P_B$ = 100 Torr) at crystal regions are greater than Sh = 17.1 ($P_B$ = 20 Torr) and Sh = 10.5 ($P_B$ = 100 Torr) at source regions by a factor of 3, respectively. The dissimilar pattern of dimensionless local Sherwood numbers for source and crystal region in Fig. 8 is likely to occur from the mass flux at interfaces, but at this point, remains unsolved

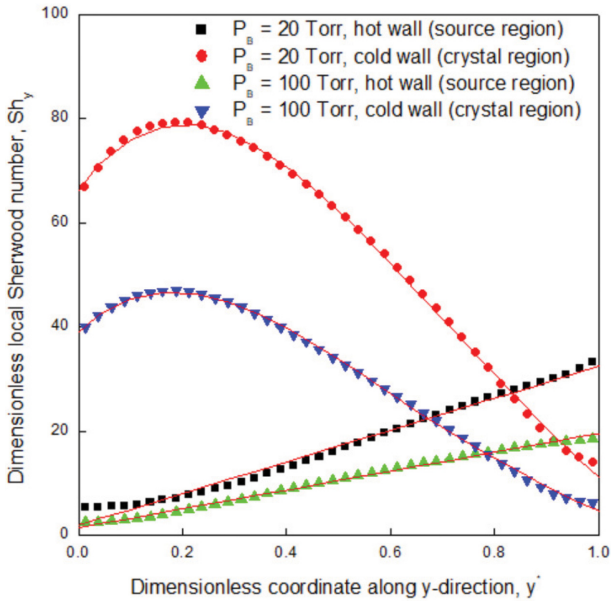


Fig. 8. Dimensionless local Sherwood number, $Sh_y$ for dimensionless coordinate along the y-direction, y* at the right hot wall (the source region) and the left cold wall (the crystal region), for $P_B = 20$ Torr and $P_B = 100$ Torr. Note that the transport parameters in Fig. 8 are the same as in Fig. 6.

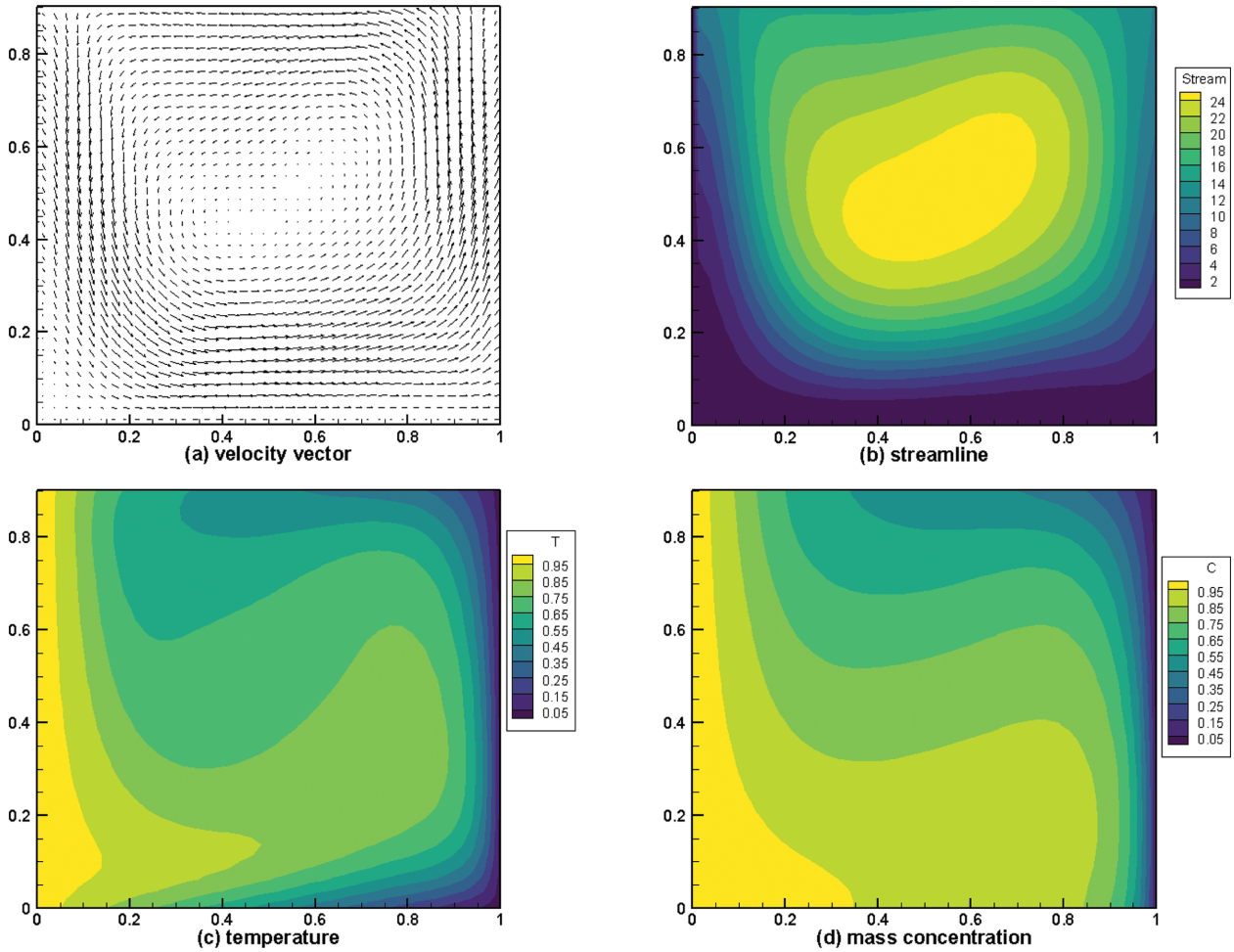


Fig. 9. (a) velocity vector, (b) streamline, (c) temperature, (d) mass concentration profile, based on $P_B = 100$ Torr, thermal Grashof number $(Gr_t) = 4.14 \times 10^3$, solutal Grashof number $(Gr_s) = 5.29 \times 10^4$, Prandtl number (Pr) = 0.89, Lewis number (Le) = 0.64, Peclet number (Pe) = 1.85, concentration parameter $(C_v) = 1.18$, $|U|_{max} = 16.68$ cm/sec, on earth. Ar = 1 and $\Delta T = 50^oC$ ($300^oC \rightarrow 250^oC$) are fixed.

problems for further researches.

Figure 9 shows velocity vectors, streamlines, iso-temperature, iso-mass concentration contours, based on $P_B$ = 100 Torr, thermal Grashof number $(Gr_t) = 4.14 \times 10^3$, solutal Grashof number $(Gr_s) = 5.29 \times 10^4$, Prandtl number (Pr) = 0.89, Lewis number (Le) = 0.64, Peclet number (Pe) = 1.85, concentration parameter $(C_v) = 1.18$, $|U|_{max} = 16.68$ cm/sec, on earth. Ar = 1 and $\Delta T = 50^oC$ ($300^oC \rightarrow 250^oC$) are fixed. With the same trend as shown in Fig. 5, Fig. 9 shows that single one convective roll appears in the vapor phase. The flow structure is asymmetrical against at y* = 0.5 and three-dimensional flow structure.

## 4. Conclusions

It is concluded that alterations of average Nusselt and average Sherwood numbers with (a) the source and crystal regions, (b) the pressures of component argon of 20 Torr and 100 Torr are analyzed and addressed in details. Both average Nusselt and average Sherwood numbers are found to decrease with increasing the partial pressures of component argon. Also, it is found that for two different partial pressures of component argon, average Nusselt numbers at the source region are greater than at the crystal region, and average Sherwood numbers at the source region augment by a factor of 3 in a comparison with the crystal region.

## Acknowledgement

One of the authors (Geug Tae Kim) would like to express much appreciation of his one year of start-up research starting him from September 1, 2020 through August 31, 2021, with which the Hannam University provided.

## References


[ 1 ] J.-Q. Yang and B.-X. Zhao, "Numerical investigation of double-diffusive convection in rectangular cavities with different aspect ratio I: High-accuracy numerical method", Comput. Math. Appl. 94 (2021) 155, https://doi.org/10.1016/j.camwa.2021.05.002.

[ 2 ] J.-T. Hu and S.-J. Me, "Unsteady double diffusive convection inside a partial porous building enclosure subjected to time-periodic temperature boundary condition", Int. Commun. Heat Mass Transf. 122 (2021) 105128, https://doi.org/10.1016/j.icheatmasstransfer.2021.105128.

[ 3 ] Z. Raizah and A.M. Aly, "Double-diffusive convection of a rotating circular cylinder in a porous cavity suspended by nano-encapsulated phase change materials", Case Studies in Thermal Eng. 24 (2021) 100864, https://doi.org/10.1016/j.csite.2021.100864.

[ 4 ] M.M. Rajabi, M. Fahs, A. Panjehfouladgaran, B. Ataie-Ashtiani, C.T. Simmons and B. Belfort, "Uncertainty quantification and global sensitivity analysis of double-diffusive natural convection in a porous enclosure", Int. J. Heat Mass Transf. 162 (2020) 120291, https://doi.org/10.1016/j.ijheatmasstransfer.2020.120291.

[ 5 ] I.S. Shivakumara, K.R. Raghunatha and G. Pallavi, "Intricacies of coupled molecular diffusion on double diffusive viscoelastic porous convection", Results in Appl. Math. 7 (2020) 100124, https://doi.org/10.1016/j.rinam.2020.100124.

[ 6 ] S. Hussain, M. Jamal and B.P. Geridonmez, "Impact of power law fluid and magnetic field on double diffusive mixed convection in staggered porous cavity considering Dufour and Soret effects", Int. Commun. Heat Mass Transf. 121 (2021) 105075, https://doi.org/10.1016/j.icheatmasstransfer.2020.105075.

[ 7 ] S. Darbhasayanam and D. Barman, "The variable gravity field and viscous dissipation effects on the double diffusive and Soret driven convective instability in a porous layer with throughflow", Int. Commun. Heat Mass Transf. 120 (2021) 105050, https://doi.org/10.1016/j.icheatmasstransfer.2020.105050.

[ 8 ] I. Filahi, M. Hasnaoui, A. Amahmid and M. Bourich, "Double-diffusive natural convection study in a shallow horizontal porous layer filled with a binary fluid and submitted to destabilized conditions in the presence of Soret effect", Mater. Today Proc. 45 (2021) 7432, https://doi.org/10.1016/j.matpr. 2021.01.685.

[ 9 ] S. Kondo, H. Gotoda, T. Miyano and I.T. Tokuda, "Chaotic dynamics of large-scale double-diffusive convection in a porous medium", Physica D: Nonlinear Phenomena 364 (2018) 1, https://doi.org/10.1016/j.physd.2017.08.011.

[10] S. Hussain, H.F. Öztop, M.A. Qureshi and N. Abu-Hamdeh, "Double diffusive buoyancy induced convection in stepwise open porous cavities filled nanofluid", Int. Commun. Heat Mass Transf. 119 (2020) 104949, https://doi.org/10.1016/j.icheatmasstransfer.2020.104949.

[11] Q. Yu, "A decoupled wavelet approach for multiple physical flow fields of binary nanofluid in double-diffusive convection", Appl. Math. Comput. 404 (2021) 126232, https://doi.org/10.1016/j.amc.2021.126232.

[12] A. Sharma, D. Tripathi, R.K. Sharma and A.K. Tiwari, "Analysis of double diffusive convection in electroosmosis regulated peristaltic transport of nanofluids", Physica A: Statistical Mechanics and its Applications 535 (2019) 122148, https://doi.org/10.1016/j.physa.2019.122148.

[13] Q. Liu, X.-B. Feng, X.-T. Xu and Y.-L. He, "Multiple-relaxation-time lattice Boltzmann model for double-diffusive convection with Dufour and Soret effects", Int. J. Heat Mass Transf. 139 (2019) 713, https://doi.org/10.1016/j.ijheatmasstransfer.2019.05.026.

[14] M. Chakkingal, R. Voigt, C.R. Kleijn and S. Kenjereš, "Effect of double-diffusive convection with cross gradients on heat and mass transfer in a cubical enclosure with adiabatic cylindrical obstacles", Int. J. Heat Fluid Flow 83 (2020) 108574, https://doi.org/10.1016/j.ijheatfluidflow.2020.108574.

[15] G.A. Meften, "Conditional and unconditional stability for double diffusive convection when the viscosity has a maximum", Appl. Math. Comput. 392 (2021) 125694, https://doi.org/10.1016/j.amc.2020.125694.

[16] S. Hamimid, M. Guellal and M. Bouafia, "Limit the buoyancy ratio in Boussinesq approximation for double-diffusive convection in binary mixture", Phys Fluids 33 (2021) 036101, https://doi.org/10.1063/5.0037320.

[17] A. Chauhan, P.M. Sahu and C. Sasmal, "Effect of polymer additives and viscous dissipation on natural convection in a square cavity with differentially heated side walls", Int. J. Heat and Mass Transf. 175 (2021) 121342, https://doi.org/10.1016/j.ijheatmasstransfer.2021.121342.

[18] G.T. Kim and M.H. Kwon, "Effects of solutally dominant convection on physical vapor transport for a mixture of $Hg_2Br_2$ and $Br_2$ under microgravity environments", Korean Chem. Eng. Res. 52 (2014) 75.

[19] G.T. Kim and M.H. Kwon, "Numerical analysis of the influences of impurity on diffusive-convection flow fields by physical vapor transport under terrestrial and microgravity conditions: with application to mercurous chloride", Appl. Chem. Eng. 27 (2016) 335.

[20] S.H. Ha and G.T. Kim, "Preliminary studies on double-diffusive natural convection during physical vapor transport crystal growth of $Hg_2Br_2$ for the spaceflight experiments", Korean Chem. Eng. Res. 57 (2019) 289.

[21] G.T. Kim and M.H. Kwon, "Double-diffusive convection affected by conductive and insulating side walls during physical vapor transport of $Hg_2Br_2$", J. Korean Cryst. Growth Cryst. Tech. 30 (2020) 117.

[22] W.M.B. Duval, "Transition to chaos in the physical transport process-I", the Proceeding of the ASME--WAM Winter Annual meeting, Fluid mechanics phenomena in microgravity, ASME-WAM, New Orleans, Louisiana (1993).

[23] J.A. Weaver and R. Viskanta, "Natural convection due to horizontal temperature and concentration gradients -1. Variable thermophysical property effects", Int. J. Heat and Mass Transf. 34 (1991) 3107.

[24] J.A. Weaver and R. Viskanta, "Natural convection due to horizontal temperature and concentration gradients -2. Species interdiffusion, Soret and Dufour effects", thermophysical property effects", Int. J. Heat and Mass Transf. 34 (1991) 3121.

[25] K.A. McCarthy, A.P. Goutzoulis, M. Gottlieb and N.B. Singh, "Optical rotatory power in crystals of the mercu-

rous halides and tellurium dioxide", Opt. Commun. 64 (1987) 157.
[26] R. Mazelsky, D.K. Fox, "Development of large single crystals for electronic, electro-optic and acousto-optic devices", Prog. Crystal Growth and Charact. 15 (1987) 75.
[27] N.B. Singh, M. Gottlieb, A.P. Goutzoulis, R.H. Hopkins and R. Mazelsky, "Mercurous Bromide acousto-optic devices", J. Cryst. Growth 89 (1988) 527.
[28] N.B. Singh, M. Marshall, M. Gottlieb, G.B. Brandt, R.H. Hopkins, R. Mazelsky, W.M.B. Duval and M.E. Glicksman, "Purification and characterization of mercurous halides", J. Cryst. Growth 106 (1990) 61.
[29] N.B. Singh, M. Gottlieb and R. Mazelsky, "The optical quality of mercurous halides crystals", J. Cryst. Growth 128 (1993) 1053.
[30] N.B. Singh, M. Gottlieb, R.H. Hopkins, R. Mazelsky, W.M.B. Duval and M.E. Glicksman "Physical vapor transport growth of mercurous chloride crystals", Prog. Crystal Growth and Charact. 27 (1993) 201.
[31] N.B. Singh, M. Gottlieb, G.B. Branddt, A.M. Stewart, R.H. Hopkins, R. Mazelsky and M.E. Glicksman, "Growth and characterization of mercurous halide crystals: mercurous bromide system", J. Cryst. Growth 137 (1994) 155.
[32] A.A. Kaplyanskii, V.V. Kulakov, Yu.F. Markov and Ĉ. Barta, "The soft mode properties in Raman spectra of improper ferroelastics $Hg_2Cl_2$ and $Hg_2Br_2$", Solid State Commun. 21 (1977) 1023.
[33] M. Dalmon, S. Nakashima, S. Komatsubara and A. Mitsuishi, "Softening of acoustic and optical modes in ferroelstic phase in $Hg_2Br_2$", Solid State Commun. 28 (1978) 815.
[34] J.S. Kim, S.B. Trivedi, J. Soos, N. Gupta and W. Palosz, "Growth of $Hg_2Cl_2$ and $Hg_2Br_2$ single crystals by physical vapor transport", J. Cryst. Growth 310 (2008) 2457.
[35] P.M. Amarasinghe, J.S. Kim, H. Chen, S. Trivedi, S.B. Qadri, J. Soos, M. Diestler, D. Zhang, N. Gupta and J.L. Jensen, "Growth of high quality mercurous halide sing crystals by physical vapor transport method for AOM and radiation detection applications", J. Cryst. Growth 450 (2016) 96.
[36] T.H. Kim, H.T. Lee, Y.M. Kang, G.E. Jang, I.H. Kwon and B. Cho, "In-depth investigation of $Hg_2Br_2$ crystal growth and evolution", Materials 12 (2019) 4224, https://doi.org/10.3390/ma12244224.
[37] L. Liu, R. Li, L. Zhang, P. Zhang, G. Zhang, S. Xia and X. Tao, "Long wavelength infrared acousto-optic crystal $Hg_2Br_2$: Growth optimization and photosensitivity investigation", J. Alloys Compd. 874 (2021) 159943, https://doi.org/10.1016/j.jallcom.2021.159943.
[38] S.V. Patankar, "Numerical Heat Transfer and Fluid Flow", (Hemisphere Publishing Corp., Washington D. C., 1980) p. 131.